ORGANOMETALLICS

pubs.acs.org/Organometallics Article

# Enantioselectivity in the Noyori–Ikariya Asymmetric Transfer Hydrogenation of Ketones

Pavel A. Dub,* Nikolay V. Tkachenko, Vijyesh K. Vyas, Martin Wills, Justin S. Smith, and Sergei Tretiak

Cite This: *Organometallics* 2021, 40, 1402–1410 Read Online

ACCESS | Metrics & More | Article Recommendations | Supporting Information

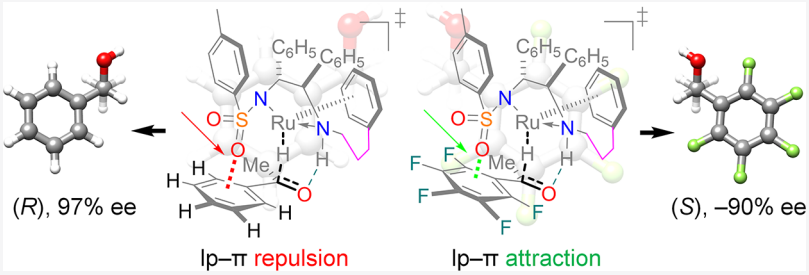


**ABSTRACT:** Asymmetric transfer hydrogenation (ATH) is an important catalytic process in the fragrance and pharmaceutical industries. The Noyori–Ikariya chiral molecular ruthenium complex has been the catalyst of choice for this reaction for over 25 years. The mechanism and origin of enantioselectivity have irked chemists ever since the catalyst conception. This work addresses important shortcomings in understanding the origin of enantioselectivity with the Noyori–Ikariya catalysts, traditionally associated with the CH–$\pi$ interaction [*Angew. Chem., Int. Ed.* **2001**, *40*, 2818]. Here, we show that there are two spatial regions of the catalyst that simultaneously control the enantioselectivity for any arbitrary substrate: the region of the (tethered) $\eta^6$-arene ligand and the region of the $SO_2$ moiety. Dynamic equilibrium and interplay of attraction and repulsion via CH–$\pi$, C–H···H–C, lone pair–$\pi$, lone pair···H–C, and other noncovalent interactions in each region lead to stabilization/destabilization of the corresponding diastereomeric transition state and, as such, determine the final percent enantiomeric excess (% ee).

## 1. INTRODUCTION

Asymmetric transfer hydrogenation (ATH) of ketones and imines represents a powerful alternative to asymmetric hydrogenation for the production of optically active alcohols and amines.[1] Specifically, the use of stable hydrogen donors such as propan-2-ol, $HCO_2Na/H_2O$, or azeotropic mixtures of $HCO_2H–NEt_3$ has an operational advantage by avoiding flammable hydrogen gas and high-pressure equipment.[2] Because of its modularity, efficiency, stability, and cost-effectiveness, the *N*-sulfonated diamine-$\eta^6$-arene Noyori–Ikariya ruthenium complex is one of the most common catalysts used in the fine chemical industry.[3] Since the publication of the first catalytic system in 1995,[4] several other variations have been developed.[5] In many cases, the enantiomeric excess (ee) in the ATH (and related AH) of ketones frequently reaches ~99%. However, such high levels of enantioselection are observed for electron-rich aromatic[4a] and alkynyl[6] ketones. In contrast, the use of perfluoroaromatic[7] and aliphatic[1a−c,e,f,5e,8] ketones leads to much smaller ee's and even reversal of the sense of the enantioselection; see Scheme 1 on the example of representative commercially available precatalysts (*R*,*R*)-**I** and (*R*,*R*)-**II**.

For a period of time,[9,10] the CH–$\pi$ interaction between the C–H proton(s) of the ($\eta^6$-arene) ligand and $\pi$ electron density of the approaching electron-rich ketonic substrate has been associated with the major interaction that contributes to the high enantioselectivity.[11] However, an ee of 99% or higher usually suggests that there is only one kinetically accessible mechanism of generation of chirality arising as a compromise of multiple attractive and repulsive (typically noncovalent) interactions between the substrate and the catalyst within the catalyst–substrate transition-state complex.[12] Specifically, lone pair(s) lp(s)–$\pi$ repulsion originating from the $SO_2$ oxygen atom(s) of the catalyst and the electron-rich aromatic substrate was further identified as another equally important factor contributing to the high enantiomeric excess for electron-rich aromatic ketones with the Noyori–Ikariya complex.[13] Up to now, however, there is no general understanding of what determines the enantioselectivity for an arbitrary prochiral ketone and/or any *N*-sulfonated diamine derivatives of the Noyori–Ikariya ruthenium catalyst. Here, based on hybrid dispersion-corrected density functional theory (DFT)[14]

**Received:** April 1, 2021
**Published:** April 27, 2021

**Scheme 1. Reported Asymmetric Transfer Hydrogenation of Acetophenone,[4a] 2′,3′,4′,5′,6′-Pentafluoroacetophenone,[7] and 1-Cyclohexylethanone[5e] with Precatalysts (*R*,*R*)-I and (*R*,*R*)-II[a,b]**

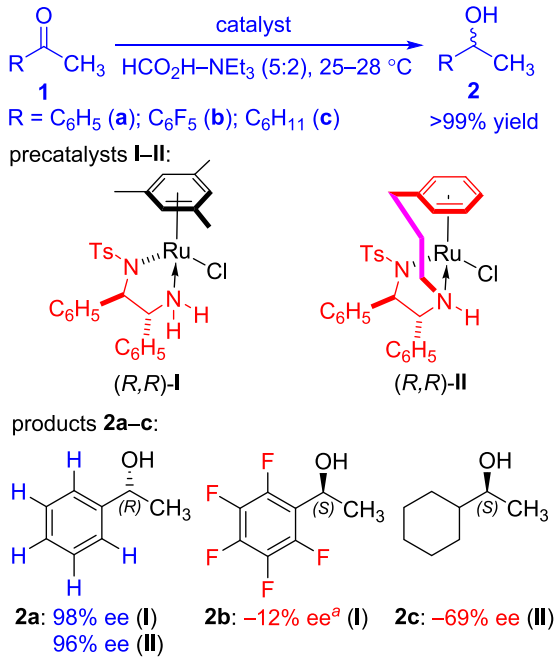


[a]*p*-Cymene version of the catalyst **I** and propan-2-ol as reagent/solvent were used for **1b**, respectively. [b]Ts = 4-$CH_3C_6H_4SO_2$.

calibrated against experimental data, we eliminate these important shortcomings in understanding the origin of enantioselectivity with the Noyori–Ikariya catalyst. Our results explain the experimentally observed drop and further reverse of the sense of the enantioselection for "challenging" perfluoroaromatic and aliphatic ketones and, more importantly, provide insights for next-generation catalyst design.

## 2. RESULTS AND DISCUSSION

**2.1. Comparative Asymmetric Transfer Hydrogenation of 1a–c with Precatalysts (*R*,*R*)-I and (*R*,*R*)-II.** To calibrate the computational results presented in this work, we performed the ATH of acetophenone (**1a**), 2′,3′,4′,5′,6′-pentafluoroacetophenone (**1b**), and 1-cyclohexylethanone (**1c**) with chiral precatalysts (*R*,*R*)-**I** and (*R*,*R*)-**II** under identical conditions in propan-2-ol (Table 1).

**Table 1. Comparative ATH of Acetophenone, 2′,3′,4′,5′,6′-Pentafluoroacetophenone, and 1-Cyclohexylethanone with Chiral Precatalysts (*R*,*R*)-I and (*R*,*R*)-II, Isopropanol, 2 mol % KOH, 25 °C, 1 mol % Precatalyst Loading[b]**

| run | substrate | precatalyst | conversion (%)[a] | % ee[a] | *R*/*S* |
|---|---|---|---|---|---|
| 1 | **1a** | (*R*,*R*)-**I** | ∼99 | 97 ± 1 | *R* |
| 2 | **1a** | (*R*,*R*)-**II** | ∼95 | 96 ± 1 | *R* |
| 3 | **1b** | (*R*,*R*)-**I** | >99 | −16 ± 2 | *S* |
| 4 | **1b** | (*R*,*R*)-**II** | >99 | −90 ± 0 | *S* |
| 5 | **1c** | (*R*,*R*)-**I** | ∼13 | −72 ± 2 | *S* |
| 6 | **1c** | (*R*,*R*)-**II** | ∼40 | −73 ± 4 | *S* |

[a]In 24 h, based on the withdrawn aliquot, chiral GC (average of 2 runs). [b][substrate] = 0.1 M, 0.5 mmol scale.

In line with the previous results where $HCO_2H$–$NEt_3$ was used as a source of hydrogen atoms and reaction media,[4a,5e] both precatalysts (*R*,*R*)-**I** and (*R*,*R*)-**II** produced (*R*)-1-phenylethanol (**2a**) with an excellent enantiomeric excess of ∼96 to 97% in the ATH of acetophenone (**1a**), runs 1–2 (Table 1). Switching to 2′,3′,4′,5′,6′-pentafluoroacetophenone (**1b**) resulted in the reverse of the sense of the enantioselection, producing (*S*)-configuration 1-(pentafluorophenyl)ethanol (**2b**) with −16 and −90% ee for precatalysts (*R*,*R*)-**I** and (*R*,*R*)-**II**, respectively (runs 3 and 4; Table 1). The sense and level of enantioselectivity of −16% observed with mesitylene precatalyst (*R*,*R*)-**I** are comparable to that of −12% reported for the similar *p*-cymene analogue.[7b] However, we note here an appreciably high level of a percent enantiomeric excess of ∼−90% for (*S*)-1-(pentafluorophenyl)-ethanol (**2b**) achieved with catalyst (*R*,*R*)-**II** in this reaction, which is a significant improvement over most existing catalytic ATH approaches[15] developed to replace classical synthetic methods.[16] The use of 1-cyclohexylethanone (**1c**) similarly results in the reverse of the sense of the enantioselection, delivering (*S*)-1-cyclohexylethanol (**2c**) with similar (assuming exponential behavior) ∼−72% ee and ∼−73% ee for (*R*,*R*)-**I** and (*R*,*R*)-**II**, respectively (runs 5 and 6; Table 1). The sense of the enantioface selection (*S*-product) and the value of ∼−73% ee for (*R*,*R*)-**II** are well comparable to the value of ∼−69% ee reported in $HCO_2H$–$NEt_3$.[5e]

**2.2. Dispersion-Corrected DFT Identification of Stereoselectivity Determining Transition States.** Dispersion-corrected DFT calculations were further used to estimate percent enantiomeric excesses and identify noncovalent interactions (NCIs) involved in four representative enantioselective reactions of (*R*,*R*)-**I**/**1a**, (*R*,*R*)-**I**/**1b**, (*R*,*R*)-**II**/**1b**, and (*R*,*R*)-**II**/**1c**. The mechanism of ATH of ketones with the Noyori–Ikariya catalyst is understood to an appreciable degree.[1b,17] The experimental and theoretical data accumulated for the asymmetric transfer hydrogenation of ketones point to two plausible catalytic cycles, which differ only in their second proton ($H^+$) transfer step.[13] The relative contribution of the pathway in which the N–H functionality remains intact is difficult to assess from the static[13] DFT computations, whereas dynamic[18] DFT computations point to propan-2-ol as the predominant source of the proton, i.e. the catalytic reaction coordinate does not asymptotically include the $16e^-$ amido Ru complex[19] on the potential energy surface. Regardless, both reaction channels are identical by the first hydride ($H^-$) step, which is rate- and enantiodetermining.[20] The composition of the enantiomers (% ee) therefore is (classically) expected to be determined by the free-energy difference ($\Delta G_{298K}^{\circ}$) between two diastereomeric transition states leading to the opposite enantiomers of the product. The stereoselectivity determining transition states can be accessed via geometry optimization using common quantum chemical methodologies.[12]

Three popular hybrid DFT exchange–correlation kernels[21] coupled with the extended def2-TZVP basis set[22] were then used to model stereoselectivity determining transition states, namely, B3LYP[23] (with the global 20% orbital exchange fraction), range-separated ωB97X-D[24] (with 100 and 22% exchanges at long and short ranges, respectively), and M06-2X[25] (with global 54% exchange) functionals. The use of dispersion-corrected models is mandatory for an improved description of noncovalent interactions (specifically van der Waals forces).[26] As such, utilized B3LYP and M06-2X functionals were parameterized via the D3 dispersion


https://doi.org/10.1021/acs.organomet.1c00201
Organometallics 2021, 40, 1402–1410

Table 2. Calculated Free-Energy Difference ($\Delta G_{298K}°$) in kcal·mol$^{-1}$ between the Transition States Leading to *S*- and *R*-Products and Percent Enantiomeric Excess (% ee) as a Function of a DFT Model Combined with Def2-TZVP Basis and SMD(Propan-2-ol) Solvent Model

| substrate | catalyst | $\Delta G_{298K}°$ (ee) B3LYP-D3 | $\Delta G_{298K}°$ (ee) $\omega$B97X-D | $\Delta G_{298K}°$ (ee) M06-2X-D3 |
|---|---|---|---|---|
| **1a** | (*R*,*R*)-**I** | 0.9 (65%) | 0.7 (51%) | 2.1 (94%) |
| **1b** | (*R*,*R*)-**I** | −0.3 (−27%) | −2.1 (−95%) | −1.0 (−70%) |
| **1b** | (*R*,*R*)-**II** | −2.7 (−98%) | −4.2 (−99.8%) | −4.0 (−99.8%) |
| **1c**$_{(eq)}$ | (*R*,*R*)-**II** | 1.6 (88%) | 1.1 (73%) | −0.9 (−66%) |

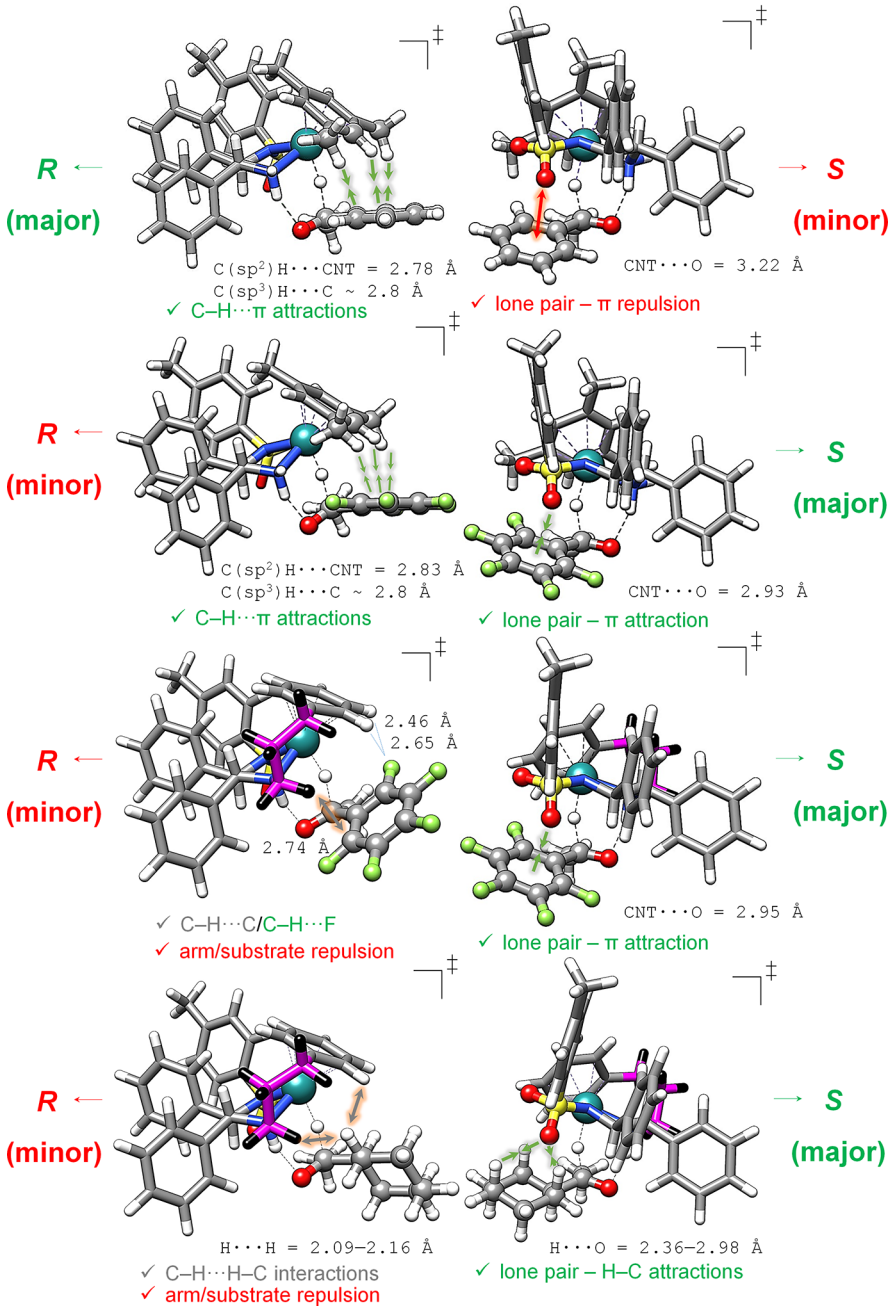


**Figure 1.** Optimized transition states at the M06-2X-D3/def2-TZVP/SMD(propan-2-ol) level leading to enantiomers of 1-phenylethanol (catalyst (*R*,*R*)-**I**, top), 1-(2,3,4,5,6-pentafluorophenyl)ethanol (catalysts (*R*,*R*)-**I** and (*R*,*R*)-**II**, middle), and 1-cyclohexane-1-ethanol (catalyst (*R*,*R*)-**II**, bottom). For (*R*,*R*)-**II**, the tethering arm is highlighted by violet. The color for various noncovalent interactions identified by finding close contacts between atoms (separation that is less than the sum of the van der Waals radii of the respective atoms) represents relative attractive (green), repulsive (red), and neutral (gray) cases.

model,[27] whereas $\omega$B97X-D implements a built-in D2 correction term.[28] Furthermore, to introduce nonspecific solvent effects of propan-2-ol in the geometry optimization steps, we employed the solvation model based on density



https://doi.org/10.1021/acs.organomet.1c00201
*Organometallics* 2021, 40, 1402−1410

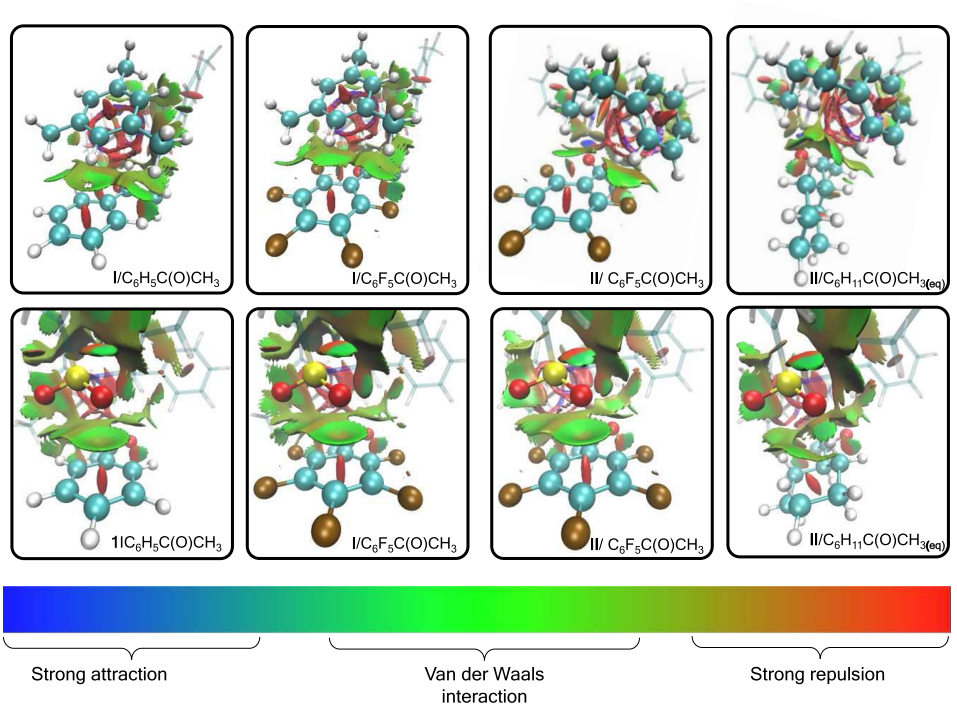


**Figure 2.** Noncovalent interaction (NCI) plots of transition states leading to enantiomers of 1-phenylethanol (catalyst (*R*,*R*)-**I**, left), 1-(2,3,4,5,6-pentafluorophenyl)ethanol (catalysts (*R*,*R*)-**I** and (*R*,*R*)-**II**, middle), and 1-cyclohexane-1-ethanol (catalyst (*R*,*R*)-**II**, right), reduced gradient of the electron density ($s$) = 0.6 au.

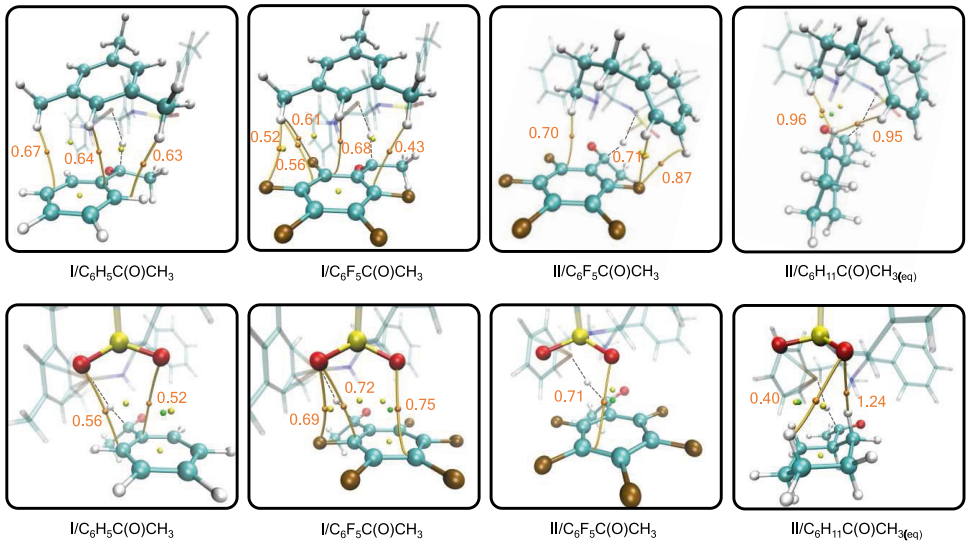


**Figure 3.** Quantum theory of atoms in molecule (QTAIM) plots of transition states leading to enantiomers of 1-phenylethanol (catalyst (*R*,*R*)-**I**, left), 1-(2,3,4,5,6-pentafluorophenyl)ethanol (catalysts (*R*,*R*)-**I** and (*R*,*R*)-**II**, middle), and 1-cyclohexane-1-ethanol (catalyst (*R*,*R*)-**II**, right). Bond paths (orange lines), bond critical points (orange small dots), ring critical points (yellow small dots), and cage critical points (green small dots). Values of electron densities ($\rho$) for bond critical points are given in [$10^{-2}$ au] units.

(SMD),[29] a popular version of a polarizable continuum model. All simulations were performed with Gaussian 16 (rev. C01) software.[30] Additional computational details and optimized geometries are provided in the SI. The results for the free-energy difference ($\Delta G_{298K}^{\circ}$) in kcal·mol$^{-1}$ between the transition states leading to *S*- and *R*-products as well as calculated from percent enantiomeric excess[31] are presented in Table 2.

The following conclusions can be made from Table 2: (1) regardless of the functional use, calculations consistently qualitatively predict[13] the correct sense of the enantioface selection for substrates **1a** and **1b**; (2) only highly advanced specifically designed to describe noncovalent interactions, M06-2X-D3 functional predicts the correct sense of the enantioface selection for substrate **1c**;[32,33] (3) on average, M06-2X-D3 being one of the most efficient dispersion-corrected hybrids according to the GMTKN30 database[34] works more effectively in terms of the sense of enantioselection and % ee prediction compared to that of B3LYP-D3 and $\omega$B97X-D.[26d,35] However, the results are only qualitative as


https://doi.org/10.1021/acs.organomet.1c00201
Organometallics 2021, 40, 1402−1410

expected due to the nonuniversal nature of the functional. In addition, the discrepancy between experimentally and theoretically predicted % ee might be affected by the additional mechanisms of the generation of chirality caused by energetically accessible conformers of the catalyst−substrate complex, the possible involvement of $Ru_R$-pathway, and specific solvation of propan-2-ol. These pathways, however, seem to play a minor role as discussed elsewhere.[17] Optimized M06-2X-D3 geometries for the transition states are shown in Figure 1.

By inspecting optimized geometries, which are first-order saddle-points on the potential energy surface, multiple close contacts defined as a separation that is less than the sum of the van der Waals radii of the respective atoms could be identified in the region of (tethered) $\eta^6$-arene ligand and the region of $SO_2$ moiety. These contacts include not only known CH−$\pi$,[36] lone pair (lp)−$\pi$,[37] and C−H···H−C interactions,[38] but also apparently a novel[39] lp···H−C noncovalent interaction ($d_{H\cdots O}$ = 2.36 Å, cf. 2.70 Å for the sum of van der Waals radii[40]). In addition, we also note several short C−H···F proximities of 2.64−2.71 Å observed for transition states leading to *R*-product of **2b** (Figure 1). To visualize noncovalent interactions present in these geometries, noncovalent interaction (NCI)[41] plots, which are based on the M06-2X-D3 electron density and its derivative analysis, were adapted (Figure 2). In all cases (i.e., eight transition states), the (green) isosurfaces confirm the presence of delocalized weak noncovalent interactions in the region of (tethered) $\eta^6$-arene ligand and the region of $SO_2$ moiety of the catalyst. The topological features of electron density in these regions were further analyzed with the well-established quantum theory of atoms in molecule (QTAIM) analysis (Figure 3).[42] The presence of noncovalent interactions is confirmed by the presence of bond critical points (BCPs) of molecular electron density. Furthermore, cage critical points (CCPs) are observed in the regions of O═S═O/arene in all three studied cases of **1a** and **1b** and are characteristic for lp−$\pi$ interactions.[43]

What causes the reverse of the sense of enantioselection when going from **1a** to **1b** with catalyst (*R*,*R*)-**I**? The analysis presented above indicates that transition states leading to *R*-product are comparably somewhat equally stabilized via CH−$\pi$ interactions (Figure 1, two top left structures). However, a large difference is observed for transition states leading to *S*-product in the region of lp−$\pi$ interactions (Figure 1, two top right structures). Although any chemical bond is a dynamic equilibrium between attractive and repulsive forces,[44] there is apparently more attraction between the lone pair of (SO)O oxygen of the catalyst and $\pi$-electron density of 2′,3′,4′,5′,6′-pentafluoroacetophenone (**1b**) vs $\pi$-electron density of acetophenone (**1a**). This is evidenced by a much shorter centroid (CNT)···O bond distance present in the case of **1b** with respect to **1a** ($\Delta$ = −0.29 Å; Figure 1), as well as greater values of electron densities ($\rho$) for bond critical points in the corresponding transition-state structures ($\Delta \sim 0.16 \times 10^{-2}$ au on average; Figure 3). More attraction implies more exergonic stabilization of the corresponding transition state, e.g., a kinetical deblockage to accumulate the *S*-enantiomer through lowering the position of the first-order saddle-point on the potential energy surface. The purely electrostatic component of these lp−$\pi$ interactions can be further understood by examining electrostatic potential (ESP)[45] maps of **1a** and **1b**, as shown in Figure 4.

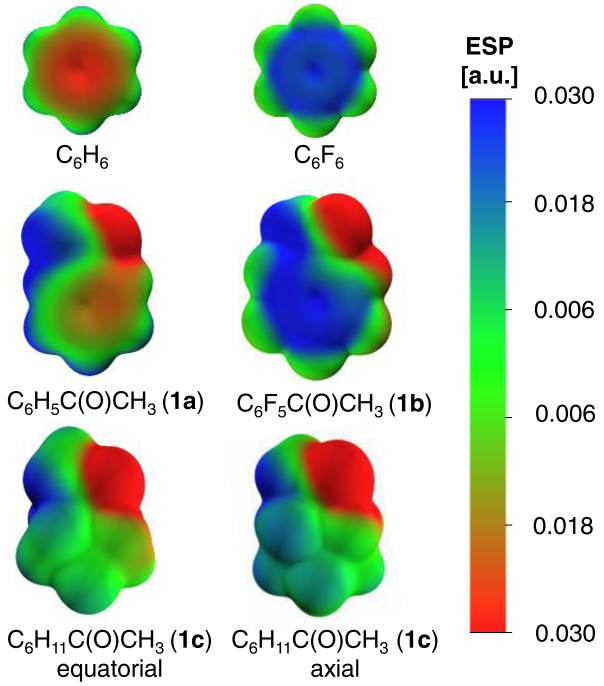


**Figure 4.** Calculated M06-2X-D3/def2-TZVP/SMD(pronan-2-ol) electrostatic potential (ESP) surfaces ($\rho$ = 0.001 au) of benzene, hexafluorobenzene, acetophenone, 2′,3′,4′,5′,6′-pentafluoroacetophenone, and two conformers of 1-cyclohexylethanone.

The $\pi$ cloud of benzene (shown for comparison) and to some extent acetophenone (**1a**) creates a negative region of ESP, called the heap, above and below the molecular plane leading to a negative sign of quadrupole moment tensor $Q_{zz}$ (*z*-direction is normal to the molecular plane) (see the SI).[46] In contrast, the similar region ("hole") of ESP is positive for hexafluorobenzene (shown for comparison) and 2′,3′,4′,5′,6′-pentafluoroacetophenone (**1b**), leading to a positive sign of quadrupole moment tensor $Q_{zz}$. One therefore should expect that the aromatic ring of **1a** will repel the negative oxygen atom of the $SO_2$ moiety of the catalyst, whereas the one of **1b** will attract it. To conclude, lp−$\pi$ interaction in the region of the $SO_2$ moiety of the catalyst seems to be the major driving force, which causes the reverse of the sense of enantioselection when going from **1a** to **1b** with catalyst (*R*,*R*)-**I**.

What makes a further dramatic improvement of the % ee for **1b** when going from catalyst (*R*,*R*)-**I** to (*R*,*R*)-**II**? The transition states leading to the major *S*-product seem to be stabilized by lp−$\pi$ interaction on an equal footing ("identical" CNT···O bond distance of ∼2.94 Å as well as a $\rho$ of $\sim 0.70 \times 10^{-2}$ au). In contrast, there seems to be more destabilization present for the diastereomeric transition state leading to a minor *R*-product with (*R*,*R*)-**II** (Figure 1, second structure from bottom right), thus kinetically blocking its accumulation. The origin of this destabilization is the "tethered" arm, which increases steric bulkiness. As a result, the aromatic ring of **1b** experiences forced rotation around the C($sp^2$)−C($sp^3$) bond. Even though the resultant structure is stabilized by C−H···X (X = C, F) interactions, the overall destabilization plays a major role. Therefore, the reason why (*R*,*R*)-**II** gives **2b** with much improved % ee than (*R*,*R*)-**I** relies on the kinetical blockage of the pathway leading to a minor *R*-product through significant destabilization of the corresponding diastereomeric transition state in the region of (tethered) $\eta^6$-arene ligand.


https://doi.org/10.1021/acs.organomet.1c00201
*Organometallics* 2021, 40, 1402−1410

Finally, computational analysis provides insights into why (*R*,*R*)-**II** reduces **3a** with the reverse of the sense of enantioselection and moderate enantioselectivity. Here, the transition state that leads to *S*-product is stabilized by lp···H−C interactions, whereas its diastereomeric counterpart that leads to *R*-product is stabilized by C−H···H−C interactions. Since these interactions seem to be comparable by force (see ESP surfaces in Figure 4), but with the non-negligible preference for *S*-pathway ($\rho$ of ∼1.24 × $10^{-2}$ vs 0.95 × $10^{-2}$ au, respectively), the final product is accumulated as *S*-enantiomer with a moderate ee of 78%.

## 3. CONCLUSIONS

The field of molecular asymmetric catalysis is of great research interest in modern catalysis science. The elucidation of the mechanism of the generation of chirality in catalytic asymmetric reactions is a central task aimed at improved catalyst design. This task is seemingly much more complex than is commonly accepted. For example, it is known that increasing the size of the catalyst often results in a higher percent enantiomeric excess.[12] However, at the moment, it is impossible to attribute this effect to any particular dominating type of intramolecular interactions because along with an evident increase of steric bulkiness, the network of possible noncovalent interactions is also increasing.[39] Hence, mechanistic studies of the chiral catalytic reactions should preferably pursue the task of accumulating and calibrating data describing the weak noncovalent interactions.[12] This work attempts to provide a comprehensive understanding of the mechanism of generation of chirality in the ATH of arbitrary prochiral ketones with the Noyori−Ikariya ruthenium catalyst being one of the most appealing examples of the use of molecular catalysts in the fine chemical industry. Thus far, CH−$\pi$ interaction in the region of ($\eta^6$-arene) ligand of the catalyst has been thought to be a major stereoregulating factor.[11] This work shows that there are actually two spatial regions of the catalyst that simultaneously control the enantioselectivity for any arbitrary substrate: the region of (tethered) $\eta^6$-arene ligand and the region of the $SO_2$ moiety. Dynamical equilibrium and interplay of attraction and repulsion via various noncovalent interactions in each region lead to stabilization/destabilization of the corresponding diastereomeric transition state and, as such, determine the final percent enantiomeric excess (% ee).

The newly established mechanism of generation of chirality with the Noyori−Ikariya catalyst explains the experimental drop and further reverse of the sense of the enantioselection for challenging perfluoroaromatic and aliphatic ketones. For the aromatic and perfluoroaromatic ketones, in particular, the enantioselectivity is largely controlled by the catalyst region of the $SO_2$ moiety, in which repulsive-to-attractive repolarization of lp−$\pi$ interactions leads to the inversion in the sense of enantioselection.

It is our hope that the results of this work will inspire the next-generation catalyst design, which still traditionally relies on the experimental trial-and-error approach. Although to the best of our knowledge no explicit examples exist of the rational catalyst design using lessons from studies of lp−$\pi$ interactions, in particular, we note that this interaction within the catalyst−substrate complex was recently used to rationalize an inversion in the sense of enantioselection in another catalytic reaction, an asymmetric fluorination of allylic alcohols.[47]

## ■ ASSOCIATED CONTENT

### Supporting Information

The Supporting Information is available free of charge at https://pubs.acs.org/doi/10.1021/acs.organomet.1c00201.

Detailed experimental procedures; characterization data; and computational details (PDF)
Coordinates.xyz (XYZ)

## ■ AUTHOR INFORMATION


### Corresponding Author

**Pavel A. Dub** − *Chemistry Division, Los Alamos National Laboratory, Los Alamos, New Mexico 87545, United States;* orcid.org/0000-0001-9750-6603; Email: pdub@lanl.gov

### Authors

**Nikolay V. Tkachenko** − *Chemistry Division, Los Alamos National Laboratory, Los Alamos, New Mexico 87545, United States; Department of Chemistry and Biochemistry, Utah State University, Logan, Utah 84322, United States;* orcid.org/0000-0002-7296-4293

**Vijyesh K. Vyas** − *Department of Chemistry, The University of Warwick, Coventry CV4 7AL, United Kingdom*

**Martin Wills** − *Department of Chemistry, The University of Warwick, Coventry CV4 7AL, United Kingdom;* orcid.org/0000-0002-1646-2379

**Justin S. Smith** − *Theoretical Division, Los Alamos National Laboratory, Los Alamos, New Mexico 87545, United States*

**Sergei Tretiak** − *Theoretical Division, Los Alamos National Laboratory, Los Alamos, New Mexico 87545, United States;* orcid.org/0000-0001-5547-3647

Complete contact information is available at: https://pubs.acs.org/10.1021/acs.organomet.1c00201


### Notes

The authors declare no competing financial interest.

## ■ ACKNOWLEDGMENTS

The work at Los Alamos National Laboratory (LANL) was supported by the LANL Directed Research and Development Funds (LDRD) and performed in part at the Center for Integrated Nanotechnologies (CINT), a U.S. Department of Energy, Office of Science user facility at LANL. The authors thank LANL Institutional Computing (IC) program for access to HPC resources. LANL is operated by Triad National Security, LLC, for the National Nuclear Security Administration of the U.S. Department of Energy (Contract No. 89233218CNA000001). The authors also thank The Royal Society (RS, U.K.) and The Science and Engineering Research Board (SERB, India) for funding V.K.V. through an SERB-Newton International Fellowship and also thank Johnson Matthey Ltd. for a gift of (*R*,*R*)-**II**.

## ■ REFERENCES

(1) (a) Barrios-Rivera, J.; Xu, Y.; Wills, M. Applications of N′-monofunctionalised TsDPEN derivatives in asymmetric catalysis. *Org. Biomol. Chem.* **2019**, *17*, 1301−1321. (b) Dub, P. A.; Gordon, J. C. The role of the metal-bound N−H functionality in Noyori-type molecular catalysts. *Nat. Rev. Chem.* **2018**, *2*, 396−408. (c) Matsunami, A.; Kayaki, Y. Upgrading and expanding the scope of homogeneous transfer hydrogenation. *Tetrahedron Lett.* **2018**, *59*, 504−513. (d) Echeverria, P.-G.; Ayad, T.; Phansavath, P.; Ratovelomanana-Vidal, V. Recent Developments in Asymmetric Hydrogenation and Transfer Hydrogenation of Ketones and Imines

through Dynamic Kinetic Resolution. *Synthesis* **2016**, *48*, 2523−2539. (e) Foubelo, F.; Nájera, C.; Yus, M. Catalytic asymmetric transfer hydrogenation of ketones: recent advances. *Tetrahedron: Asymmetry* **2015**, *26*, 769−790. (f) Ikariya, T.; Blacker, A. J. Asymmetric Transfer Hydrogenation of Ketones with Bifunctional Transition Metal-Based Molecular Catalysts. *Acc. Chem. Res.* **2007**, *40*, 1300−1308.

(2) (a) Wu, X.; Wang, C.; Xiao, J. Transfer Hydrogenation in Water. *Chem. Rec.* **2016**, *16*, 2772−2786. (b) Wei, Y.; Wu, X.; Wang, C.; Xiao, J. Transfer hydrogenation in aqueous media. *Catal. Today* **2015**, *247*, 104−116. (c) Wang, D.; Astruc, D. The Golden Age of Transfer Hydrogenation. *Chem. Rev.* **2015**, *115*, 6621−6686.

(3) (a) Cotman, A. E. Escaping from Flatland: Stereoconvergent Synthesis of Three-Dimensional Scaffolds via Ruthenium(II)-Catalyzed Noyori−Ikariya Transfer Hydrogenation. *Chem. - Eur. J.* **2021**, *27*, 39−53. (b) Ayad, T.; Phansavath, P.; Ratovelomanana-Vidal, V. Transition-Metal-Catalyzed Asymmetric Hydrogenation and Transfer Hydrogenation: Sustainable Chemistry to Access Bioactive Molecules. *Chem. Rec.* **2016**, *16*, 2754−2771. (c) Cotarca, L.; Verzini, M.; Volpicelli, R. Catalytic asymmetric transfer hydrogenation: an industrial perspective. *Chim. Oggi* **2014**, *32*, 36−42.

(4) (a) Fujii, A.; Hashiguchi, S.; Uematsu, N.; Ikariya, T.; Noyori, R. Ruthenium(II)-Catalyzed Asymmetric Transfer Hydrogenation of Ketones Using a Formic Acid−Triethylamine Mixture. *J. Am. Chem. Soc.* **1996**, *118*, 2521−2522. (b) Uematsu, N.; Fujii, A.; Hashiguchi, S.; Ikariya, T.; Noyori, R. Asymmetric Transfer Hydrogenation of Imines. *J. Am. Chem. Soc.* **1996**, *118*, 4916−4917.

(5) (a) Dub, P. A.; Matsunami, A.; Kuwata, S.; Kayaki, Y. Cleavage of N−H Bond of Ammonia via Metal−Ligand Cooperation Enables Rational Design of a Conceptually New Noyori−Ikariya Catalyst. *J. Am. Chem. Soc.* **2019**, *141*, 2661−2677. (b) G. Nedden, H.; Zanotti-Gerosa, A.; Wills, M. The Development of Phosphine-Free 'Tethered' Ruthenium(II) Catalysts for the Asymmetric Reduction of Ketones and Imines. *Chem. Rec.* **2016**, *16*, 2623−2643. (c) Touge, T.; Hakamata, T.; Nara, H.; Kobayashi, T.; Sayo, N.; Saito, T.; Kayaki, Y.; Ikariya, T. Oxo-Tethered Ruthenium(II) Complex as a Bifunctional Catalyst for Asymmetric Transfer Hydrogenation and H2 Hydrogenation. *J. Am. Chem. Soc.* **2011**, *133*, 14960−14963. (d) Li, C.; Villa-Marcos, B.; Xiao, J. Metal−Brønsted Acid Cooperative Catalysis for Asymmetric Reductive Amination. *J. Am. Chem. Soc.* **2009**, *131*, 6967−6969. (e) Hayes, A. M.; Morris, D. J.; Clarkson, G. J.; Wills, M. A Class of Ruthenium(II) Catalyst for Asymmetric Transfer Hydrogenations of Ketones. *J. Am. Chem. Soc.* **2005**, *127*, 7318−7319.

(6) (a) Vyas, V. K.; Knighton, R. C.; Bhanage, B. M.; Wills, M. Combining Electronic and Steric Effects To Generate Hindered Propargylic Alcohols in High Enantiomeric Excess. *Org. Lett.* **2018**, *20*, 975−978. (b) Reddy, K.S.N.; Sabitha, G. First total synthesis of Pestalotioprolide C and its C7 epimer. *Tetrahedron Lett.* **2017**, *58*, 1198−1201. (c) Brandt, D.; Dittoo, A.; Bellosta, V.; Cossy, J. Synthetic Approach to Wortmannilactone C. *Org. Lett.* **2015**, *17*, 816−819. (d) Arai, N.; Satoh, H.; Utsumi, N.; Murata, K.; Tsutsumi, K.; Ohkuma, T. Asymmetric Hydrogenation of Alkynyl Ketones with the $\eta^6$-Arene/TsDPEN−Ruthenium(II) Catalyst. *Org. Lett.* **2013**, *15*, 3030−3033. (e) Matsumura, K.; Hashiguchi, S.; Ikariya, T.; Noyori, R. Asymmetric Transfer Hydrogenation of $\alpha$, $\beta$-Acetylenic Ketones. *J. Am. Chem. Soc.* **1997**, *119*, 8738−8739.

(7) (a) Šterk, D.; Stephan, M.; Mohar, B. Highly Enantioselective Transfer Hydrogenation of Fluoroalkyl Ketones. *Org. Lett.* **2006**, *8*, 5935−5938. (b) Brandt, P.; Roth, P.; Andersson, P. G. Origin of Enantioselectivity in the Ru(arene)(amino alcohol)-Catalyzed Transfer Hydrogenation of Ketones. *J. Org. Chem.* **2004**, *69*, 4885−4890.

(8) (a) Cheung, F. K.; Lin, C.; Minissi, F.; Crivillé, A. L.; Graham, M. A.; Fox, D. J.; Wills, M. An Investigation into the Tether Length and Substitution Pattern of Arene-Substituted Complexes for Asymmetric Transfer Hydrogenation of Ketones. *Org. Lett.* **2007**, *9*, 4659−4662. (b) Soni, R.; Collinson, J.-M.; Clarkson, G. C.; Wills, M. An Unexpected Directing Effect in the Asymmetric Transfer Hydrogenation of $\alpha$,$\alpha$-Disubstituted Ketones. *Org. Lett.* **2011**, *13*, 4304−4307.

(9) (a) Chen, F.; He, D.; Chen, L.; Chang, X.; Wang, D. Z.; Xu, C.; Xing, X. Chirality-Economy Catalysis: Asymmetric Transfer Hydrogenation of Ketones by Ru-Catalysts of Minimal Stereogenicity. *ACS Catal.* **2019**, *9*, 5562−5566. (b) Wang, W.; Yang, X. Mechanistic insights into asymmetric transfer hydrogenation of pyruvic acid catalysed by chiral osmium complexes with formic acid assisted proton transfer. *Chem. Commun.* **2019**, *55*, 9633−9636. (c) Matsuoka, A.; Sandoval, C. A.; Uchiyama, M.; Noyori, R.; Naka, H. Why p-Cymene? Conformational Effect in Asymmetric Hydrogenation of Aromatic Ketones with a $\eta^6$-Arene/Ruthenium(II) Catalyst. *Chem. Asian J.* **2015**, *10*, 112−115.

(10) (a) Touge, T.; Sakaguchi, K.; Tamaki, N.; Nara, H.; Yokozawa, T.; Matsumura, K.; Kayaki, Y. Multiple Absolute Stereocontrol in Cascade Lactone Formation via Dynamic Kinetic Resolution Driven by the Asymmetric Transfer Hydrogenation of Keto Acids with Oxo-Tethered Ruthenium Catalysts. *J. Am. Chem. Soc.* **2019**, *141*, 16354−16361. (b) Touge, T.; Arai, T. Asymmetric Hydrogenation of Unprotected Indoles Catalyzed by $\eta^6$-Arene/N-Me-sulfonyldiamine−Ru(II) Complexes. *J. Am. Chem. Soc.* **2016**, *138*, 11299−11305. (c) Cotman, A. E.; Cahard, D.; Mohar, B. Stereoarrayed $CF_3$-Substituted 1,3-Diols by Dynamic Kinetic Resolution: Ruthenium-(II)-Catalyzed Asymmetric Transfer Hydrogenation. *Angew. Chem., Int. Ed.* **2016**, *55*, 5294−5298. (d) Rast, S.; Modec, B.; Stephan, M.; Mohar, B. $\gamma$-Sultam-cored N,N-ligands in the ruthenium(ii)-catalyzed asymmetric transfer hydrogenation of aryl ketones. *Org. Biomol. Chem.* **2016**, *14*, 2112−2120.

(11) Yamakawa, M.; Yamada, I.; Noyori, R. CH/$\pi$ Attraction: The Origin of Enantioselectivity in Transfer Hydrogenation of Aromatic Carbonyl Compounds Catalyzed by Chiral $\eta^6$-Arene-Ruthenium(II) Complexes. *Angew. Chem., Int. Ed.* **2001**, *40*, 2818−2821.

(12) Gridnev, I. D.; Dub, P. A. *Enantioselection in Asymmetric Catalysis*; CRC Press, 2016.

(13) Dub, P. A.; Ikariya, T. Quantum Chemical Calculations with the Inclusion of Nonspecific and Specific Solvation: Asymmetric Transfer Hydrogenation with Bifunctional Ruthenium Catalysts. *J. Am. Chem. Soc.* **2013**, *135*, 2604−2619.

(14) (a) Grimme, S. Density functional theory with London dispersion corrections. *WIRES Comput. Mol. Sci.* **2011**, *1*, 211−228. (b) Kohn, W.; Sham, L. J. Self-Consistent Equations Including Exchange and Correlation Effects. *Phys. Rev.* **1965**, *140*, A1133−A1138. (c) Hohenberg, P.; Kohn, W. Inhomogeneous Electron Gas. *Phys. Rev.* **1964**, *136*, B864−B871.

(15) (a) Zheng, L.; Yin, X.; Mohammadlou, A.; Sullivan, R. P.; Guan, Y.; Staples, R.; Wulff, W. D. Asymmetric Catalytic Meerwein−Ponndorf−Verley Reduction of Ketones with Aluminum(III)-VANOL Catalysts. *ACS Catal.* **2020**, *10*, 7188−7194. (b) Brüning, F.; Nagae, H.; Käch, D.; Mashima, K.; Togni, A. Asymmetric Hydrogenation of Aryl Perfluoroalkyl Ketones Catalyzed by Rhodium(III) Monohydride Complexes Bearing Josiphos Ligands. *Chem. - Eur. J.* **2019**, *25*, 10818−10822. (c) Szőllősi, G.; Kolcsár, V. J. Highly Enantioselective Transfer Hydrogenation of Prochiral Ketones Using Ru(II)-Chitosan Catalyst in Aqueous Media. *ChemCatChem* **2019**, *11*, 820−830. (d) Mejía, E.; Aardoom, R.; Togni, A. Asymmetric Transfer Hydrogenation of Ketones Catalyzed by Rhenium Complexes with Chiral Ferrocenylphosphane Ligands. *Eur. J. Inorg. Chem.* **2012**, *2012*, 5021−5032. (e) Nakamura, K.; Yamanaka, R.; Tohi, K.; Hamada, H. Cyanobacterium-catalyzed asymmetric reduction of ketones. *Tetrahedron Lett.* **2000**, *41*, 6799−6802.

(16) Xu, H.; Chen, B. A kind of synthetic method of optical voidness phenyl-pentafluoride ethanol. CN106957212A2017.

(17) Dub, P. A.; Gordon, J. C. The mechanism of enantioselective ketone reduction with Noyori and Noyori−Ikariya bifunctional catalysts. *Dalton Trans.* **2016**, *45*, 6756−6781.

(18) (a) Pavlova, A.; Meijer, E. J. Understanding the Role of Water in Aqueous Ruthenium-Catalyzed Transfer Hydrogenation of Ketones. *ChemPhysChem* **2012**, *13*, 3492−3496. (b) Handgraaf, J.-W.; Meijer, E. J. Realistic Modeling of Ruthenium-Catalyzed Transfer Hydrogenation. *J. Am. Chem. Soc.* **2007**, *129*, 3099−3103.



https://doi.org/10.1021/acs.organomet.1c00201
*Organometallics* 2021, 40, 1402−1410

(19) Haack, K.-J.; Hashiguchi, S.; Fujii, A.; Ikariya, T.; Noyori, R. The Catalyst Precursor, Catalyst, and Intermediate in the $Ru^{II}$-Promoted Asymmetric Hydrogen Transfer between Alcohols and Ketones. *Angew. Chem., Int. Ed.* **1997**, *36*, 285−288.
(20) In this work, the chlorido precursors shown in Figure 1 are referred to as precatalysts, whereas the corresponding hydrido complexes generated in situ under the catalytic reaction conditions are referred to as catalysts. See Ref.'s [1b] and [17] for more details.
(21) (a) Qi, S.-C.; Hayashi, J.-i.; Zhang, L. Recent application of calculations of metal complexes based on density functional theory. *RSC Adv.* **2016**, *6*, 77375−77395. (b) Tekarli, S. M.; Drummond, M. L.; Williams, T. G.; Cundari, T. R.; Wilson, A. K. Performance of Density Functional Theory for 3d Transition Metal-Containing Complexes: Utilization of the Correlation Consistent Basis Sets. *J. Phys. Chem. A* **2009**, *113*, 8607−8614. (c) Cramer, C. J.; Truhlar, D. G. Density functional theory for transition metals and transition metal chemistry. *Phys. Chem. Chem. Phys.* **2009**, *11*, 10757−10816. (d) Zhao, Y.; Truhlar, D. G. Density Functionals with Broad Applicability in Chemistry. *Acc. Chem. Res.* **2008**, *41*, 157−167.
(22) (a) Weigend, F.; Ahlrichs, R. Balanced basis sets of split valence, triple zeta valence and quadruple zeta valence quality for H to Rn: Design and assessment of accuracy. *Phys. Chem. Chem. Phys.* **2005**, *7*, 3297−3305. (b) Weigend, F. Accurate Coulomb-fitting basis sets for H to Rn. *Phys. Chem. Chem. Phys.* **2006**, *8*, 1057−1065.
(23) Stephens, P. J.; Devlin, F. J.; Chabalowski, C. F.; Frisch, M. J. Ab Initio Calculation of Vibrational Absorption and Circular Dichroism Spectra Using Density Functional Force Fields. *J. Phys. Chem. A* **1994**, *98*, 11623−11627.
(24) Chai, J.-D.; Head-Gordon, M. Long-range corrected hybrid density functionals with damped atom-atom dispersion corrections. *Phys. Chem. Chem. Phys.* **2008**, *10*, 6615−6620.
(25) Zhao, Y.; Truhlar, D. G. The M06 suite of density functionals for main group thermochemistry, thermochemical kinetics, noncovalent interactions, excited states, and transition elements: two new functionals and systematic testing of four M06-class functionals and 12 other functionals. *Theor. Chem. Acc.* **2008**, *120*, 215−241.
(26) (a) Stöhr, M.; Van Voorhis, T.; Tkatchenko, A. Theory and practice of modeling van der Waals interactions in electronic-structure calculations. *Chem. Soc. Rev.* **2019**, *48*, 4118−4154. (b) DiLabio, G. A.; Otero-de-la-Roza, A. Noncovalent Interactions in Density Functional Theory. In *Reviews in Computational Chemistry*; Parrill, A. L.; Lipkowitz, K. B., Eds.; John Wiley & Sons, Inc., 2016; pp 1−97. (c) Sun, J.; Remsing, R. C.; Zhang, Y.; Sun, Z.; Ruzsinszky, A.; Peng, H.; Yang, Z.; Paul, A.; Waghmare, U.; Wu, X.; Klein, M. L.; Perdew, J. P. Accurate first-principles structures and energies of diversely bonded systems from an efficient density functional. *Nat. Chem.* **2016**, *8*, 831−836. (d) Corminboeuf, C. Minimizing Density Functional Failures for Non-Covalent Interactions Beyond van der Waals Complexes. *Acc. Chem. Res.* **2014**, *47*, 3217−3224.
(27) Grimme, S.; Antony, J.; Ehrlich, S.; Krieg, H. A consistent and accurate ab initio parametrization of density functional dispersion correction (DFT-D) for the 94 elements H-Pu. *J. Chem. Phys.* **2010**, *132*, No. 154104.
(28) Grimme, S. Semiempirical GGA-type density functional constructed with a long-range dispersion correction. *J. Comput. Chem.* **2006**, *27*, 1787−1799.
(29) Marenich, A. V.; Cramer, C. J.; Truhlar, D. G. Universal Solvation Model Based on Solute Electron Density and on a Continuum Model of the Solvent Defined by the Bulk Dielectric Constant and Atomic Surface Tensions. *J. Phys. Chem. B* **2009**, *113*, 6378−6396.
(30) Frisch, M. J.; Trucks, G. W.; Schlegel, H. B.; Scuseria, G. E.; Robb, M. A.; Cheeseman, J. R.; Scalmani, G.; Barone, V.; Petersson, G. A.; Nakatsuji, H.; Li, X.; Caricato, M.; Marenich, A. V.; Bloino, J.; Janesko, B. G.; Gomperts, R.; Mennucci, B.; Hratchian, H. P.; Ortiz, J. V.; Izmaylov, A. F.; Sonnenberg, J. L.; Williams-Young, D.; Ding, F.; Lipparini, F.; Egidi, F.; Goings, J.; Peng, B.; Petrone, A.; Henderson, T.; Ranasinghe, D.; Zakrzewski, V. G.; Gao, J.; Rega, N.; Zheng, G.; Liang, W.; Hada, M.; Ehara, M.; Toyota, K.; Fukuda, R.; Hasegawa, J.; Ishida, M.; Nakajima, T.; Honda, Y.; Kitao, O.; Nakai, H.; Vreven, T.; Throssell, K.; Montgomery, J. A., Jr.; Peralta, J. E.; Ogliaro, F.; Bearpark, M. J.; Heyd, J. J.; Brothers, E. N.; Kudin, K. N.; Staroverov, V. N.; Keith, T. A.; Kobayashi, R.; Normand, J.; Raghavachari, K.; Rendell, A. P.; Burant, J. C.; Iyengar, S. S.; Tomasi, J.; Cossi, M.; Millam, J. M.; Klene, M.; Adamo, C.; Cammi, R.; Ochterski, J. W.; Martin, R. L.; Morokuma, K.; Farkas, O.; Foresman, J. B.; Fox, D. J. *Gaussian 16*, revision C.01; Gaussian, Inc.: Wallingford CT, 2016.
(31) ee (%)= $100 \times [\exp(-\Delta G_{298K^\circ}/RT) - 1]/[\exp(-\Delta G_{298K^\circ}/RT) + 1]$, where $\Delta G_{298K^\circ}$ is the free-energy difference in kcal·mol$^{-1}$ between the transition states leading to *S*- and *R*-products, $RT$ = 0.59 kcal·mol$^{-1}$.
(32) 1-cyclohexylethanone undergoes a conformational interconversion known as a chair flip [33]. In this chair flip, all axial groups become equatorial and all equatorial groups become axial. Both chair forms of 1-cyclohexylethanone were considered in our calculations (see the SI). Transition states leading to 1-cyclohexylethanol were found to be uniformly ∼2−7 few kcal·mol$^{-1}$ more stable for the chair conformation of 1-cyclohexylethanone, which has an equatorial C(O)$CH_3$ group, in line with the stability of this conformer relative to the axial configuration by −0.58 kcal·mol$^{-1}$ (M06-2X-D3) (see the SI).
(33) Jensen, F. R.; Bushweller, C. H.; Beck, B. H. Conformational preferences in monosubstituted cyclohexanes determined by nuclear magnetic resonance spectroscopy. *J. Am. Chem. Soc.* **1969**, *91*, 344−351.
(34) Goerigk, L.; Grimme, S. A thorough benchmark of density functional methods for general main group thermochemistry, kinetics, and noncovalent interactions. *Phys. Chem. Chem. Phys.* **2011**, *13*, 6670−6688.
(35) (a) Reilly, A. M.; Tkatchenko, A. Understanding the role of vibrations, exact exchange, and many-body van der Waals interactions in the cohesive properties of molecular crystals. *J. Chem. Phys.* **2013**, *139*, No. 024705. (b) Johnson, E. R.; Salamone, M.; Bietti, M.; DiLabio, G. A. Modeling Noncovalent Radical−Molecule Interactions Using Conventional Density-Functional Theory: Beware Erroneous Charge Transfer. *J. Phys. Chem. A* **2013**, *117*, 947−952.
(36) Nishio, M. The CH/$\pi$ hydrogen bond in chemistry. Conformation, supramolecules, optical resolution and interactions involving carbohydrates. *Phys. Chem. Chem. Phys.* **2011**, *13*, 13873−13900.
(37) (a) Novotný, J.; Bazzi, S.; Marek, R.; Kozelka, J. Lone-pair−$\pi$ interactions: analysis of the physical origin and biological implications. *Phys. Chem. Chem. Phys.* **2016**, *18*, 19472−19481. (b) Geboes, Y.; De Proft, F.; Herrebout, W. A. Lone pair···$\pi$ interactions involving an aromatic $\pi$-system: Complexes of hexafluorobenzene with dimethyl ether and trimethylamine. *Chem. Phys. Lett.* **2016**, *647*, 26−30. (c) Singh, S. K.; Das, A. The n → $\pi^*$ interaction: a rapidly emerging non-covalent interaction. *Phys. Chem. Chem. Phys.* **2015**, *17*, 9596−9612. (d) Mooibroek, T. J.; Gamez, P.; Reedijk, J. Lone pair−$\pi$ interactions: a new supramolecular bond? *CrystEngComm* **2008**, *10*, 1501−1515.
(38) (a) Chen, J.; Gridnev, I. D. Size is Important: Artificial Catalyst Mimics Behavior of Natural Enzymes. *iScience* **2020**, *23*, No. 100960. (b) Khavasi, H. R.; Balmohammadi, Y.; Naghavi, S. S. Phenomenal Observation of Attractive Intermolecular CH···HC Interaction in a Mercury (II) Complex: An Experimental and First-Principles Study. *ChemistrySelect* **2019**, *4*, 10246−10253. (c) Rösel, S.; Quanz, H.; Logemann, C.; Becker, J.; Mossou, E.; Cañadillas-Delgado, L.; Caldeweyher, E.; Grimme, S.; Schreiner, P. R. London Dispersion Enables the Shortest Intermolecular Hydrocarbon H···H Contact. *J. Am. Chem. Soc.* **2017**, *139*, 7428−7431.
(39) Neel, A. J.; Hilton, M. J.; Sigman, M. S.; Toste, F. D. Exploiting non-covalent $\pi$ interactions for catalyst design. *Nature* **2017**, *543*, 637−646.
(40) Alvarez, S. A cartography of the van der Waals territories. *Dalton Trans.* **2013**, *42*, 8617−8636.
(41) (a) Johnson, E. R.; Keinan, S.; Mori-Sánchez, P.; Contreras-García, J.; Cohen, A. J.; Yang, W. Revealing Noncovalent Interactions. *J. Am. Chem. Soc.* **2010**, *132*, 6498−6506. (b) Contreras-García, J.;


https://doi.org/10.1021/acs.organomet.1c00201
*Organometallics* 2021, 40, 1402−1410

Johnson, E. R.; Keinan, S.; Chaudret, R.; Piquemal, J.-P.; Beratan, D. N.; Yang, W. NCIPLOT: A Program for Plotting Noncovalent Interaction Regions. *J. Chem. Theory Comput.* **2011**, *7*, 625−632.
(42) Bader, R. F. W. A quantum theory of molecular structure and its applications. *Chem. Rev.* **1991**, *91*, 893−928.
(43) (a) Kashyap, C.; Ullah, S. S.; Mazumder, L. J.; Kanti Guha, A. Non-covalent interaction in benzene and substituted benzene: A theoretical study. *Comput. Theor. Chem.* **2018**, *1130*, 134−139. (b) Garau, C.; Frontera, A.; Quiñonero, D.; Ballester, P.; Costa, A.; Deyà, P. M. A Topological Analysis of the Electron Density in Anion−$\pi$ Interactions. *ChemPhysChem* **2003**, *4*, 1344−1348.
(44) R. Zohar, A.; Levy, S. T. Attraction vs. repulsion − learning about forces and energy in chemical bonding with the ELI-Chem simulation. *Chem. Educ. Res. Pract.* **2019**, *20*, 667−684.
(45) Murray, J. S.; Sen, K. Molecular Electrostatic Potentials: Concepts and Applications. In *Theoretical and Computational Chemistry*; Elsevier, 1996; pp 1−665.
(46) Battaglia, M. R.; Buckingham, A. D.; Williams, J. H. The electric quadrupole moments of benzene and hexafluorobenzene. *Chem. Phys. Lett.* **1981**, *78*, 421−423.
(47) Neel, A. J.; Milo, A.; Sigman, M. S.; Toste, F. D. Enantiodivergent Fluorination of Allylic Alcohols: Data Set Design Reveals Structural Interplay between Achiral Directing Group and Chiral Anion. *J. Am. Chem. Soc.* **2016**, *138*, 3863−3875.

## NOTE ADDED AFTER ASAP PUBLICATION

This paper was originally published on April 27, 2021 with incorrect versions of the abstract graphic and Figure 1. A corrected version was resposted on April 28, 2021.


https://doi.org/10.1021/acs.organomet.1c00201
*Organometallics* 2021, 40, 1402−1410